CHINESE OPTICS LETTERS

Vol. 20, No. 11 | November 2022

Inversely-designed terahertz metadevice with ultrafast modulation of double electromagnetically induced transparency windows

Siyang Hu (胡思扬)[1], Cheng Xiang'ai (程湘爱)[1], Weibao He (何韦宝)[1], Yuze Hu (胡瑜泽)[2], Mingyu Tong (童明玉)[1], and Zhongjie Xu (许中杰)[1*]

[1] College of Advanced Interdisciplinary Studies, National University of Defense Technology, Changsha 410073, China

[2] Beijing Institute for Advanced Study, National University of Defense Technology, Beijing 100020, China

*Corresponding author: zhongjie_xu@qq.com

Received April 5, 2022 | Accepted June 6, 2022 | Posted Online July 13, 2022

Terahertz metasurfaces have great applications for efficient terahertz modulation, but there are still problems in designing terahertz metadevices in terms of complexity and inefficiency. Herein, we demonstrate an inversely-designed terahertz metasurface with double electromagnetically induced transparency (EIT)-like windows by incorporating a particle swarm optimization (PSO) algorithm with the finite-difference time-domain method. We prepared and tested the metadevices, and the experimental terahertz signals are close to the designed results. By hybridizing amorphous germanium film with the inversely-designed metasurface, two EIT-like windows, including transmission and slow-light effect, exhibit ultrafast modulation behavior in 25 ps excited by a femtosecond laser. The modulation depths of transmission in two transparency windows are 74% and 65%, respectively. The numerical simulations also illustrate the ultrafast dynamic process and modulation mechanism, which match well with the experiment results. Our work thus offers opportunities for designing other objective functions of the terahertz metadevice.

Keywords: terahertz metasurfaces; inverse design; double electromagnetically induced transparency.
DOI: 10.3788/COL202220.113701

1. Introduction

As of late, the metasurface-based electromagnetically induced transparency (EIT) analog has drawn in impressive consideration, attributed to an assortment of promising applications in the field of quantum information storage[1–3], novel optical communication[4,5], slow-light devices[6–8], and sensing[9–11]. Usually, in metasurfaces, the EIT effect has been obtained via the near-field coupling between bright and dark modes or super-radiant and sub-radiant modes[12–17]. The common method of generating and regulating the EIT effect in metasurfaces is to utilize split-ring resonators (SRRs) by adjusting the position and distance between resonators in a unit cell[8,13,18–20]. Nevertheless, most studies about the metasurface-based EIT effect are limited to a single narrow transparency window, which greatly restricts the extent of EIT metasurface applications. Accordingly, metasurface-based EIT effects with multiple bands are significant for future applications in the terahertz (THz) regime. The dual-EIT effect exhibits two transparency windows, indicating dual-channel coding applications[21,22]. Normally, the double-band EIT in metasurfaces can be realized by coupling of the bright and dark modes, with the metasurface composed of two metal wires and a double SRR[23]. The demand for adjusting and optimizing numbers of geometry parameters to achieve the desired goal is complicated and professional. Thus, it is significant to search for simple and universal methods to design double EIT.

The inverse design scheme is advised to set up unconventional functions and structures. Concerning the inverse design, the whole design process can be handed over to computer machines, requiring less metasurface expertise and manual involvement[24–29]. For the given functionality of the THz metadevice, the inverse design method can obtain the corresponding geometrical parameters by optimizing the algorithm to solve the design problem. General inverse design optimization methods include but are not limited to genetic algorithm[30–32], topology optimization[33–35], direct-binary-search algorithm[36,37], and particle swarm optimization (PSO)[38–41]. With fewer parameters to adjust and the simple principle for ease of implementation, the PSO algorithm stands out from the others. In addition, fast convergence and few requirements of computer performance are the reasons for its popularity[41]. In our previous

work, we used PSO to inversely design a THz EIT-like metadevice and experimentally verified its functionality with good results, which pointed out the direction of designing metadevices with a multichannel THz transparency window and coding[42].

In this paper, we design a metasurface structure to realize double EIT-like windows by incorporating the PSO algorithm with the finite-difference time-domain (FDTD) method. To simplify the fabrication of the metasurface, we appropriately adjust interconnections between the sub-structures, so the final metasurface is easy to manufacture, but the transparent window has not been changed. Combining with amorphous germanium (Ge) film, both windows show ultrafast modulation behavior in 25 ps under the optical excitation, with a modulation depth of 74% and 65%, respectively. The ultrafast THz double EIT-like modulation is experimentally testified via optical pump THz probe technology (OPTP). Besides, the transient simulation results are also demonstrated, which match well with the experimental data. Finally, the simulation of near-field distributions explains the formation and modulation process of double EIT. Our work may be applied more generally to other objective functions and further reveals the feasibility of inversely designing a wide variety of THz metadevices.

2. Methods

To inversely design the THz metasurface supported by the dual-EIT effect, PSO algorithm combining with the FDTD method is used for optimized design. The inversely-designed structure along with the unit cell of the metasurface is composed of a stable cut wire and the surrounding pixels. The length (along the y direction) and width (along the x direction) of the cut wire are 100 and 10 μm. Each pixel is made up of two rectangular orthogonal intersections that are 3 μm wide and 5 μm high. The material of the metasurface is gold with a thickness of 200 nm (the electric conductivity $\sigma = 4.56 \times 10^7$ S/m). The entire metasurface is constructed on a quartz substrate with a refractive index of 1.98. In the FDTD simulation, the THz wave is polarized in the y direction with normal incidence, and its transmission is monitored. Periodic boundary conditions are set in both the x and y directions (p_x = 140 μm, p_y = 180 μm). A perfect matching layer (PML) is adopted in the z direction to prevent electromagnetic wave reflection at the boundary. According to the coupled mode theory (CMT), a transmission spectral curve with a dual-EIT shape can be computed by employing the following model[43]:

$$\frac{1}{2\pi}\frac{\partial}{\partial t}\begin{pmatrix} a_p \\ a_q \\ a_m \end{pmatrix} = -i\left[\begin{pmatrix} f_p+\kappa_{pp} & \kappa_{pq} & \kappa_{pm} \\ \kappa_{qp} & f_p+\kappa_{qq} & \kappa_{qm} \\ \kappa_{pm} & k_{qm} & f_m+\kappa_{mm} \end{pmatrix} - i\begin{pmatrix} \gamma_p' & 0 & 0 \\ 0 & \gamma_q' & 0 \\ 0 & 0 & \gamma_m' \end{pmatrix}\right] \times \begin{pmatrix} a_p \\ a_q \\ a_m \end{pmatrix} + \begin{pmatrix} -\gamma_p & X_{pq} & X_{pm} \\ X_{pq} & -\gamma_q & X_{qm} \\ X_{pm} & X_{qm} & -\gamma_m \end{pmatrix}\begin{pmatrix} a_p \\ a_q \\ a_m \end{pmatrix} + \begin{pmatrix} d_{1p} & d_{2p} \\ d_{1q} & d_{2q} \\ d_{1m} & d_{2m} \end{pmatrix} S^+. \tag{1}$$

Here, a_l ($l = p, q, m$) denotes the amplitudes of three modes. f_l is the resonance frequency of modes. γ_l and γ_l' denote the radiation and absorption losses of modes, respectively. κ_i and X_i ($i = pq, pm, qm$) account for, respectively, the near-field and far-field coupling between every two modes. d_i describes the coupling between external light and modes. κ_s ($s = pp, qq, mm$) denotes the on-site correction by the perturbation. S^+ denotes the incident excitation. Check Ref. [43] for detailed derivation. Through standard CMT analyses and appropriate parameters adjustments, we get the transmission curves as black dot line in Fig. 1(b). As for the inverse design process, at the beginning, we constructed a 28×36 matrix layout, where each cell corresponds to a pixel. A Boolean value of "1" or "0" is set on each cell to indicate the presence or absence of the pixel. Then, through the program, we gave a random initial value and optimized it by the PSO algorithm so that the THz responses get close to the target curve. Along with multiple iterations of the PSO algorithm, the position and number of pixels are constantly updated until the simulated transmission curve is close to the target curve and no longer changes, that is convergence. The final structure is shown in Fig. 1(a). Note that it is not unique, and it is just one of many structures that meet the conditions, which means that the inversely-designed structure is diverse. The target curve and final result of the inverse design are depicted in Fig. 1(b), from which we can see that the inverse-design result matches well with our intended goals. For ease of facilitated processing, appropriate adjustments to the unit cell

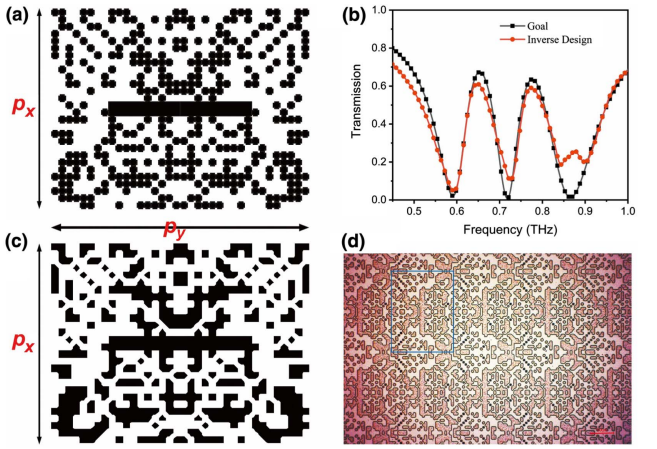

Fig. 1. (a) Original inversely-designed structure, where p_x and p_y are the periods in the x and y direction, respectively. (b) The transmission spectra of the target (black) and inverse design (red). (c) Adjusted inverse design metasurface structure. (d) Processed ultimate inverse design metasurface with 200-nm-thick amorphous Ge film covering the face. The scale bar in the pictures is 50 μm.

of the metasurface structure are allowed without affecting the target transmission curve. The adjusted metasurface unit is shown in Fig. 1(c). The optical microscope diagram of the processed array is shown in Fig. 1(d). The blue box shows the structure of a periodic unit. The scale bar is 50 μm. To actively control the THz EIT effect, a 200-nm-thick amorphous Ge film was thermally evaporated on the metasurface as a photoconductive semiconductor.

3. Results

3.1. Active terahertz double EIT modulation

The THz transmission spectra in the finally designed metasurface are shown in Fig. 2(a); the simulation and experiment results match well, and both describe two EIT-like windows at 0.68 THz (peak1) and 0.77 THz (peak2). In the experimental measurements, we employ a THz time-domain system (TDS) to obtain the time-domain spectrum, and the frequency-domain spectrum is obtained by Fourier transform. A Ti:sapphire regenerative amplifier system is employed to generate a femtosecond pulse of 1 kHz repetition at a central wavelength of 800 nm for stimulating the ZnTe crystal for THz generation and detection as well as activating the photogenerated carrier of Ge film. The transmission spectrum is defined by $T = |E_S/E_R|^2$, where E_R is the transmission amplitude of the substrate, and E_S is that of the metasurface. The time-domain THz spectrum of the inversely-designed metasurface described in Fig. 2(b) shows a tail compared with that of the substrate, revealing the interplay between the THz wave and metasurface. Active dual-channel THz modulation in the EIT-like window was performed [Fig. 2(c)] by various pump fluences from 0 to 2.25 mJ/cm^2, accompanied

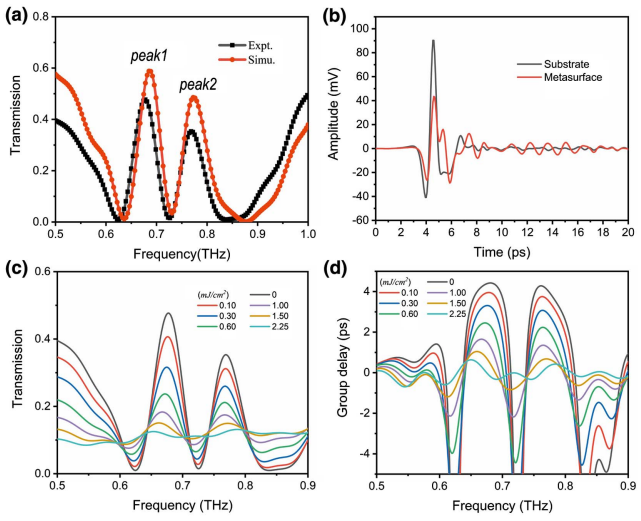

Fig. 2. (a) Experimental (black) and simulated (red) transmission spectra of the ultimate inverse design metasurface. (b) Time-domain THz spectra when the THz pulse passes the quartz substrate (black) and metasurface (red). Experimental modulation of THz double EIT (c) transmission and (d) group delay for various pump fluences ranging from 0 to 2.25 mJ/cm^2.

with the double EIT-like resonances gradually vanishing and the transmission spectrum flattening. The transparent window at peak1 was tuned from 0.47 to 0.12, with 74% modulation depth. Transmission spectra at peak2 are tuned from 0.35 to 0.12 with 65% modulation depth. The modulation depth of THz transmission was defined by MD $= \left[(T_P - T_N)/T_N\right] \times 100\%$[44], where T_P and T_N are the transmissions with and without pump light, respectively. The experimental results prompt the application of a dual-channel synchronous switch function. As a significant physical phenomenon on account of the EIT effect, the slow-light performance is shown in Fig. 2(d). Generally, we define the slow light as the group delay $\Delta t_g = -\mathrm{d}\varphi/\mathrm{d}\omega$, where $\omega = 2\pi f$ is the THz angle frequency. The positive group delay at the EIT-like window describes the slow-light effect. In regard to slow-light modulation, the group delay was tuned from around 4 to 0 ps with the pump fluence from 0 to 2.25 mJ/cm^2, showing the same modulation trend as the transmission. These experimental results strongly demonstrate the significant potential of the inversely-designed metasurface cooperating with semiconductors in transmission and slow-light switches.

3.2. Ultrafast terahertz transmission and slow-light switching

Turning now, we discuss the dynamically tunable THz EIT-like response of the inversely-designed metasurface cooperating with amorphous Ge film. Benefiting from the ultrafast relaxation time of amorphous Ge film, the THz EIT-like modulation cycle is on the picosecond scale[44,45]. To better understand the modulation process, we experimentally demonstrate the transmission and slow-light switching in Figs. 3(c) and 3(e), with the pump fluence of 2.25 mJ/cm^2, by taking advantage of OPTP. By altering the relative time delay stage between pump pulse and THz wave, the time-domain THz transmission and group delay are obtained. From the contour maps, we can see that the entire modulation period lasts around 25 ps, that is, both EIT-like windows (peak1 and peak2) completed the process from disappearance to recovery in 25 ps. Without losing generality, we simulate the modulation process to reproduce the experimental results. Before this, we employ the OPTP to measure the differential transmittance of 200 nm pure Ge film, $-\Delta T/T$, shown as Fig. 3(a), to obtain its carrier relaxation time and transient photoconductivity. Precisely, the transient photoconductivity can be extracted by the following equation[46]:

$$\Delta\sigma(t) = -\frac{\varepsilon_0 c(1+n_s)}{d_1}\frac{\Delta T}{T}(t), \tag{2}$$

where ε_0 is the permittivity of vacuum, $c = 3 \times 10^8$ m/s is the vacuum speed of light, n_s is the refractive index of substrate, and $d_1 = 200$ nm is the thickness of Ge film. Here, we set the initial conductivity of Ge film as zero, and the transient photoconductivity can be easily obtained by Eq. (2). In Fig. 3(b), under the femtosecond laser pumping, photogenerated conductivity of Ge film lasted around 7 ps, and the maximum transient

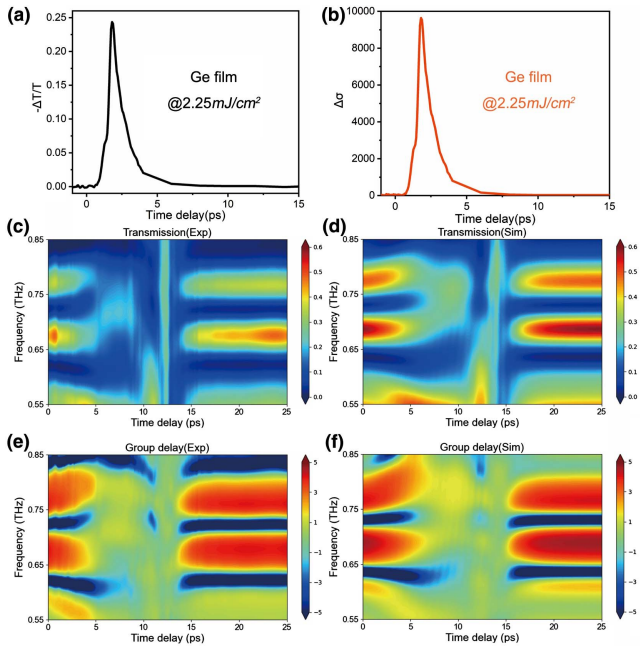

Fig. 3. Experimentally extracted (a) differential transmittance and (b) transient conductivity of 200 nm pure Ge film at pump fluence of 2.25 mJ/cm^2. (c), (e) Map of experimental THz transmission and group delay as a function of relative time delay between the femtosecond laser and THz pulse. (d), (f) Map of simulated THz transmission and group delay as a function of relative time delay between the femtosecond laser and THz pulse.

conductance is enabled near 10^4 S/m. Then, experimental data including transient conductance and THz time-domain spectrum are simulated in the inversely-designed metasurface structure. The ultrafast dynamics process of THz transmission and group delay switching in simulation are demonstrated in Figs. 3(d) and 3(f), which match well with the experimental results.

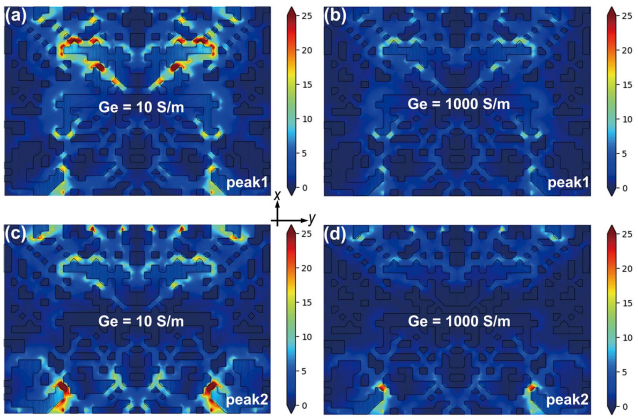

Fig. 4. Static near-field simulation results. (a), (b) Near-field distributions of the inversely-designed metasurface in the first transparency window (peak1) with various conductivities of Ge film, 10 and 1000 S/m, respectively. (c), (d) Near-field distributions of the inversely-designed metasurface in the second transparency window (peak2) with various conductivities of Ge film, 10 and 1000 S/m, respectively.

3.3. Near-field distributions of inversely-designed metasurface with various Ge conductivities

To reveal the physical mechanism of double EIT-like resonance and its modulation in inversely-designed metasurface combining with amorphous Ge film, the simulated near-field distributions with different Ge conductivities were monitored at 1 μm above the metasurface. In the static simulation, the conductivity of Ge film stays the same during the whole time-domain simulation (different from transient simulation). In the case of low conductivity of Ge film, i.e., 10 S/m, which was slightly tuned but still held double EIT-like resonance, the local electric field showed strong enhancement. As we can see in Figs. 4(a) and 4(c), the electric field is locally above at the frequency of peak1, and there is also a strong locality above the structure at the frequency of peak2 but more concentration below. The cut wire provides a radiation mode with weak local-field enhancement. The electric fields are localized at different positions reflecting different dark resonance modes, and double EIT-like resonances are found in the macroscopic transmission spectrum at last. Notably, it is a possibility to design multiple EIT-like resonances by adjusting the position of pixels based on the inverse design. On the other hand, in the case of high conductivity of Ge film, i.e., 1000 S/m, in which the double EIT-like resonance was completely suppressed, the intensity of the local electric field weakened, as shown in Figs. 4(b) and 4(d). Weakened electric-field intensity indicates a weakening of the THz coupling to the metasurface, which explains the THz EIT-like modulation based on light-excited semiconductors very well.

4. Conclusion

In conclusion, we proposed a dual-channel THz modulator via an inversely-designed metasurface combining with Ge film. With the PSO algorithm cooperating with the FDTD method, we designed a metasurface structure with double EIT-like windows. Combined with an actively tunable semiconductor, amorphous Ge film, this metadevice enables ultrafast modulation speed of 25 ps under optical excitation. Two channels achieve 74% and 65% modulation depth, respectively. Our transient simulation results are in good agreement with the experimental test data, and near-field distributions in static simulation explain the double EIT-like modulation process. The experimental and simulated results illustrate an application of two-channel ultrafast THz encoding. Our inverse design method provides a reference for designing metadevices and points the way for high-performance THz multifunctional devices.

Acknowledgement

This work was supported by the National Natural Science Foundation of China (No. 62075240) and the National Key Research and Development Program of China (No. 2020YFB2205800).

References

1. L. Wang, J.-X. Sun, M.-X. Luo, Y.-H. Sun, X.-X. Wang, Y. Chen, Z.-H. Kang, H.-H. Wang, J.-H. Wu, and J.-Y. Gao, "Image routing via atomic spin coherence," Sci. Rep. **5**, 18179 (2015).
2. L. Chen, Z. Xu, W. Zeng, Y. Wen, S. Li, and H. Wang, "Controllably releasing long-lived quantum memory for photonic polarization qubit into multiple spatially-separate photonic channels," Sci. Rep. **6**, 33959 (2016).
3. L. Fan, K. Y. Fong, M. Poot, and H. X. Tang, "Cascaded optical transparency in multimode-cavity optomechanical systems," Nat. Commun. **6**, 5850 (2015).
4. X. Yang, B. Xue, J. Zhang, and S. Zhu, "A universal quantum information processor for scalable quantum communication and networks," Sci. Rep. **4**, 6629 (2014).
5. Y.-L. Chuang, R.-K. Lee, and A. Y. Ite, "Generation of quantum entanglement based on electromagnetically induced transparency media," Opt. Express **29**, 3928 (2021).
6. X. He, X. Yang, G. Lu, W. Yang, F. Wu, Z. Yu, and J. Jiang, "Implementation of selective controlling electromagnetically induced transparency in terahertz graphene metamaterial," Carbon **123**, 668 (2017).
7. Y. Hu, T. Jiang, J. Zhou, H. Hao, H. Sun, H. Ouyang, M. Tong, Y. Tang, H. Li, and J. You, "Ultrafast terahertz transmission/group delay switching in photoactive WSe_2-functionalized metaphotonic devices," Nano Energy **68**, 104280 (2020).
8. Y. Zhao, Q. Huang, H. Cai, X. Lin, H. He, H. Cheng, T. Ma, and Y. Lu, "Ultrafast control of slow light in THz electromagnetically induced transparency metasurfaces," Chin. Opt. Lett. **19**, 073602 (2021).
9. T. Ma, Q. Huang, H. He, Y. Zhao, X. Lin, and Y. Lu, "All-dielectric metamaterial analogue of electromagnetically induced transparency and its sensing application in terahertz range," Opt. Express **27**, 16624 (2019).
10. L. Zhu, H. Li, L. Dong, W. Zhou, M. Rong, X. Zhang, and J. Guo, "Dual-band electromagnetically induced transparency (EIT) terahertz metamaterial sensor," Opt. Mater. Express **11**, 2109 (2021).
11. C. Liu, P. Liu, C. Yang, Y. Lin, and S. Zha, "Dynamic electromagnetically induced transparency based on a metal-graphene hybrid metamaterial," Opt. Mater. Express **8**, 1132 (2018).
12. Y. Hu, T. Jiang, H. Sun, M. Tong, J. You, X. Zheng, Z. Xu, and X. Cheng, "Ultrafast frequency shift of electromagnetically induced transparency in terahertz metaphotonic devices," Laser Photonics Rev. **14**, 1900338 (2020).
13. Y. Hu, M. Tong, Z. Xu, X. Cheng, and T. Jiang, "Spatiotemporal terahertz metasurfaces for ultrafast all-optical switching with electric-triggered bistability," Laser Photonics Rev. **15**, 2000456 (2021).
14. Y.-Y. Ji, F. Fan, M. Chen, L. Yang, and S.-J. Chang, "Terahertz artificial birefringence and tunable phase shifter based on dielectric metasurface with compound lattice," Opt. Express **25**, 11405 (2017).
15. K. Liu, X. Chen, M. Lian, J. Jia, Y. Su, H. Ren, S. Zhang, Y. Xu, J. Chen, Z. Tian, and T. Cao, "Nonvolatile reconfigurable electromagnetically induced transparency with terahertz chalcogenide metasurfaces," Laser Photonics Rev. **16**, 2100393 (2022).
16. H. Yao, Z. Sun, X. Yan, M. Yang, L. Liang, G. Ma, J. Gao, T. Li, X. Song, H. Zhang, Q. Yang, X. Hu, Z. Wang, Z. Li, and J. Yao, "Ultrasensitive, light-induced reversible multidimensional biosensing using THz metasurfaces hybridized with patterned graphene and perovskite," Nanophotonics **11**, 1219 (2022).
17. T. Zhou, S. Chen, X. Zhang, X. Zhang, H. Hu, and Y. Wang, "Electromagnetically induced transparency based on a carbon nanotube film terahertz metasurface," Opt. Express **30**, 15436 (2022).
18. R. Yang, Q. Fu, Y. Fan, W. Cai, K. Qiu, W. Zhang, and F. Zhang, "Active control of EIT-like response in a symmetry-broken metasurface with orthogonal electric dipolar resonators," Photonics Res. **7**, 955 (2019).
19. Y. Hu, M. Tong, Z. Xu, X. Cheng, and T. Jiang, "Bifunctional spatiotemporal metasurfaces for incident angle-tunable and ultrafast optically switchable electromagnetically induced transparency," Small **17**, 2006489 (2021).
20. Z. Bai, Q. Zhang, and G. Huang, "Nonlinear polaritons in metamaterials with plasmon-induced transparency," Chin. Opt. Lett. **17**, 012501 (2019).
21. J. Hwang, Y. Kim, Y. Yoo, K. Kim, J. Rhee, L. Chen, S. Li, X. Guo, and Y. Lee, "Tunable quad-band transmission response, based on single-layer metamaterials," Opt. Express **26**, 31607 (2018).
22. K. Zhang, C. Wang, L. Qin, R.-W. Peng, D.-H. Xu, X. Xiong, and M. Wang, "Dual-mode electromagnetically induced transparency and slow light in a terahertz metamaterial," Opt. Lett. **39**, 3539 (2014).
23. S. Hu, H. Yang, S. Han, X. Huang, and B. Xiao, "Tailoring dual-band electromagnetically induced transparency in planar metamaterials," J. Appl. Phys. **117**, 043107 (2015).
24. S. Molesky, Z. Lin, A. Y. Piggott, W. Jin, J. Vucković, and A. W. Rodriguez, "Inverse design in nanophotonics," Nat. Photonics **12**, 659 (2018).
25. S. So, T. Badloe, J. Noh, J. Rho, and J. Bravo-Abad, "Deep learning enabled inverse design in nanophotonics," Nanophotonics **9**, 1041 (2020).
26. D. Rafique and L. Velasco, "Machine learning for network automation: overview, architecture, and applications [Invited Tutorial]," J. Opt. Commun. Netw. **10**, D126 (2018).
27. S. D. Campbell, D. Sell, R. P. Jenkins, E. B. Whiting, J. A. Fan, and D. H. Werner, "Review of numerical optimization techniques for meta-device design," Opt. Mater. Express **9**, 1842 (2019).
28. B. Shen, P. Wang, R. Polson, and R. Menon, "An integrated-nanophotonics polarization beamsplitter with 2.4×2.4 μm^2 footprint," Nat. Photonics **9**, 378 (2015).
29. C. M. Lalau-Keraly, S. Bhargava, O. D. Miller, and E. Yablonovitch, "Adjoint shape optimization applied to electromagnetic design," Opt. Express **21**, 21693 (2013).
30. M. D. Huntington, L. J. Lauhon, and T. W. Odom, "Subwavelength lattice optics by evolutionary design," Nano Lett. **14**, 7195 (2014).
31. P. R. Wiecha, C. Majorel, C. Girard, A. Cuche, V. Paillard, O. L. Muskens, and A. Arbouet, "Design of plasmonic directional antennas via evolutionary optimization," Opt. Express **27**, 29069 (2019).
32. Z. Yu, H. Cui, and X. Sun, "Genetic-algorithm-optimized wideband on-chip polarization rotator with an ultrasmall footprint," Opt. Lett. **42**, 3093 (2017).
33. Z. Lin, X. Liang, M. Lončar, S. G. Johnson, and A. W. Rodriguez, "Cavity-enhanced second-harmonic generation via nonlinear-overlap optimization," Optica **3**, 233 (2016).
34. Y. Yan, P. Liu, X. Zhang, and Y. Luo, "Photonic crystal topological design for polarized and polarization-independent band gaps by gradient-free topology optimization," Opt. Express **29**, 24861 (2021).
35. Z. Lin, V. Liu, R. Pestourie, and S. G. Johnson, "Topology optimization of freeform large-area metasurfaces," Opt. Express **27**, 15765 (2019).
36. B. Shen, P. Wang, R. Polson, and R. Menon, "Ultra-high-efficiency metamaterial polarizer," Optica **1**, 356 (2014).
37. X. Ju, G. Zhu, F. Huang, Z. Dai, Y. Chen, C. Guo, L. Deng, and X. Wang, "Reverse design of pixel-type terahertz band-pass filters," Opt. Express **30**, 957 (2022).
38. Y. Zhang, S. Yang, A. Eu-Jin Lim, G.-Q. Lo, C. Galland, T. Baehr-Jones, and M. Hochberg, "A compact and low loss Y-junction for submicron silicon waveguide," Opt. Express **21**, 1310 (2013).
39. J. C. Mak, C. Sideris, J. Jeong, A. Hajimiri, and J. K. Poon, "Binary particle swarm optimized 2 x 2 power splitters in a standard foundry silicon photonic platform," Opt. Lett. **41**, 3868 (2016).
40. J. Li, L. Bao, S. Jiang, Q. Guo, D. Xu, B. Xiong, G. Zhang, and F. Yi, "Inverse design of multifunctional plasmonic metamaterial absorbers for infrared polarimetric imaging," Opt. Express **27**, 8375 (2019).
41. R. Hassan, B. Cohanim, O. de Weck, and G. Venter, "A comparison of particle swarm optimization and the genetic algorithm," in *46th AIAA/ASME/ASCE/AHS/ASC Structures, Structural Dynamics and Materials Conference, Structures, Structural Dynamics, and Materials and Co-located Conferences* (American Institute of Aeronautics and Astronautics, 2005).
42. W. He, M. Tong, Z. Xu, Y. Hu, X. Cheng, and T. Jiang, "Ultrafast all-optical terahertz modulation based on an inverse-designed metasurface," Photonics Res. **9**, 1099 (2021).
43. W. Huang, J. Lin, M. Qiu, T. Liu, Q. He, S. Xiao, and L. Zhou, "A complete phase diagram for dark-bright coupled plasmonic systems: applicability of Fano's formula," Nanophotonics **9**, 3251 (2020).
44. W. X. Lim, M. Manjappa, Y. K. Srivastava, L. Cong, A. Kumar, K. F. MacDonald, and R. Singh, "Ultrafast all-optical switching of germanium-based flexible metaphotonic devices," Adv. Mater. **30**, 1705331 (2018).
45. Y. Hu, H. Hao, J. Zhang, M. Tong, X. Cheng, and T. Jiang, "Anisotropic temporal metasurfaces for tunable ultrafast photoactive switching dynamics," Laser Photonics Rev. **15**, 2100244 (2021).
46. H. J. Joyce, J. L. Boland, C. L. Davies, S. A. Baig, and M. B. Johnston, "A review of the electrical properties of semiconductor nanowires: insights gained from terahertz conductivity spectroscopy," Semicond. Sci. Technol. **31**, 103003 (2016).